ACS APPLIED MATERIALS & INTERFACES

Research Article

www.acsami.org

Fabrication of Optical Multilayer Devices from Porous Silicon Coatings with Closed Porosity by Magnetron Sputtering

Jaime Caballero-Hernández,[†] Vanda Godinho,*[,†] Bertrand Lacroix,[†] Maria C. Jiménez de Haro,[†] Damien Jamon,[‡] and Asunción Fernández[†]

[†]Laboratory for Nanostructured Materials and Microstructure, Instituto de Ciencia de Materiales de Sevilla CSIC-Univ. Sevilla, Av. Américo Vespucio 49, 41092 Sevilla, Spain

[‡]Université de Lyon, CNRS UMR5516, Laboratoire Hubert Curien, Université Jean Monnet, 18, Rue Benoit Lauras, 42000 Saint Etienne, France

Supporting Information

ABSTRACT: The fabrication of single-material photonic-multilayer devices is explored using a new methodology to produce porous silicon layers by magnetron sputtering. Our bottom-up methodology produces highly stable amorphous porous silicon films with a controlled refractive index using magnetron sputtering and incorporating a large amount of deposition gas inside the closed pores. The influence of the substrate bias on the formation of the closed porosity was explored here for the first time when He was used as the deposition gas. We successfully simulated, designed, and characterized Bragg reflectors and an optical microcavity that integrates these porous layers. The sharp interfaces between the dense and porous layers combined with the adequate control of the refractive index and thickness allowed for excellent agreement between the simulation and the experiments. The versatility of the magnetron sputtering technique allowed for the preparation of these structures for a wide range of substrates such as polymers while also taking advantage of the oblique angle deposition to prepare Bragg reflectors with a controlled lateral gradient in the stop band wavelengths.

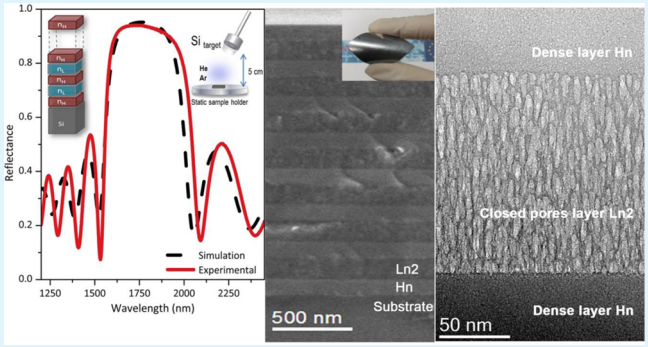

KEYWORDS: *porous silicon, magnetron sputtering, Bragg reflector, optical microcavity, lateral gradient*

INTRODUCTION

Over the past decade, the ability to tailor the refractive index (n) of porous silicon combined with its full compatibility in the microelectronics industry has provided great possibilities for its use in different fields. Single-material optical-multilayered devices, such as rugate filters, Bragg reflectors, or microcavities, have been produced with alternating porous silicon layers with different porosities and refractive indices. The refractive index (n) modulation and the structure of these multilayers produces optical interference effects in which light propagation is completely or partially inhibited (photonic band gap) at defined wavelength ranges.[1]

Porous silicon is most often fabricated using electrochemical methods in which a silicon wafer is placed in an HF-based electrolyte.[2] By adjusting the current and time, highly porous and low porosity layers with low and high refractive indexes, respectively, can be consecutively produced to obtain the optical structures.[3−8] However, some limitations can be attributed to the electrochemical process that compromises the quality of the optical response of these structures. Specifically, the anisotropy of the etching rates during the porous silicon formation increases as a function of depth as the layer is formed, and the chemical instability of the high porous layers leads to their easy oxidation.[9] To improve the chemical stabilization, thermal annealing processes have been proposed.[9−11]

We have recently presented a new bottom-up methodology to produce highly stable amorphous porous silicon layers with a controlled refractive index using magnetron sputtering.[12,13] The use of He as the working gas produces a singular microstructure with an occluded porosity[14] that can be aligned in the magnetron direction[12,13] in which the shape and size of the pores remains unaltered throughout the coating thickness. Closed porosity structures are quite stable and avoid the disadvantages, such as aging effects, of chemically etched layers.[12,15] The introduction of porosity provides a significant reduction in the refractive index of amorphous silicon coatings in comparison with dense coatings (n_{porous} = 3.75 and n_{dense} = 4.75 at 500 nm).[12]

Received: March 17, 2015
Accepted: June 5, 2015
Published: June 5, 2015

DOI: 10.1021/acsami.5b02356
ACS Appl. Mater. Interfaces 2015, 7, 13889−13897

Table 1. Deposition Conditions of the Individual Layers

coating	working gas	pressure (Pa)	bias (V)	deposition rate[a] (nm/sec)	composition RBS (at. %) Si	He	Ar	ϕ^b
H_n	Ar	1.5	−100	0.69	94.0		6	
L_{n1}	He	4.8		0.25	66	34		38.9
L_{n2}	He	8.4	−100	0.18	63	37		41.5

[a]Calculated by SEM cross sections. [b]Porosity fraction calculated according to the Maxwell−Garnet eq 1 from n values at 1750 nm.

Here, our goal is to determine the feasibility of producing silicon-photonic structures that are based on one-dimensional (1D) layers using magnetron sputtering via the sequential deposition of these materials. Magnetron sputtering is a versatile technique that allows the controlled deposition over large areas of a wide range of substrates, such as glass, steel, or even sensible or flexible substrates (polymers), and it is easy to scale up to industrial processes.

Here, we show how easily single-material distributed Bragg refractors (DBR) or optical microcavities (OMC) can be produced using magnetron sputtering by alternating the dense- and closed-porosity silicon layers in the same batch, just by changing the deposition gas and conserving the sharp interfaces. The simulation, design, and analysis of the optical multilayers are discussed. A complete analysis of the individual materials that compose the devices is presented. Because of the optical absorption range of silicon, the photonic structures developed in this work are centered in the near-IR region, making them suitable for filters that can be used at these wavelengths or in optical communications.

Typically, porous photonic structures that are based on 1D layers are produced over rigid substrates; however, recent works point to the relevance of developing flexible silicon photonic crystals.[16] For many applications, the production of these flexible electronic devices requires complicated lift-off procedures[17] or expensive lithography processes.[16] As a proof-of-concept, a multilayer system deposited on polymers is presented, which widens the potential applications for these structures that are produced by our bottom-up methodology.

An interesting characteristic of the oblique angle deposition geometry is the gradual decrease in the thickness of the coatings with the increased distance to the magnetron. Because the photonic band gap position depends on the optical thickness of the layers, we exploit the ability to prepare thinly layered stacks with similar and controlled thickness gradients as a simple and inexpensive method to prepare single-material-gradient Bragg refractors with a large range of reflectance peaks.

EXPERIMENTAL SECTION

1. Preparation of the Coatings and Characterization of the Individual Layers. To produce amorphous silicon DRB or OMC devices, individual amorphous silicon layers with a high refractive index contrast were prepared and investigated first. Thus, a dense layer with a high refractive index (H_n) and two porous candidates with a low n (L_{n1}, L_{n2}) were individually deposited using magnetron sputtering. Table 1 shows the deposition conditions of these layers. For all experiments, the magnetron head (2″ ION'X magnetron from Thin Film Consulting, Germany) was placed at a 30° angle to the normal of the sample holder and at a distance of 5 cm from the substrates, as indicated in Figure 1. The coatings were deposited from a pure Si target (Kurt J. Lesker, 99.999% pure) using a radio frequency sputtering source at a 150 W power. Silicon (100), glass, and quartz were used as the substrates. To obtain a dense coating, argon was used as the working gas, and a substrate bias of −100 V direct current was applied. For the porous coatings, the introduction of a closed porosity

Figure 1. Experimental setup.

was achieved when He was used as the deposition gas. For details, see ref 12. The two investigated low n porous layers were prepared according to Table 1 with He as the deposition gas with and without the application of a bias.

For the design of the DBR and the OMC, the dense and porous layers were alternated so that the deposited porous layers were subjected to the applied bias during the deposition of the next dense layer.

The composition of the thin films was evaluated using Rutherford proton backscattering spectrometry (p-RBS) at the National Center of Accelerators (CNA, Sevilla, Spain) using a 3 MV tandem accelerator.

The morphology and thickness of the coatings were studied using scanning electron microscopy (HITACHI S-4800 SEM-FEG). The samples were cleaved from coatings grown onto silicon and were observed without metallization in cross-sectional views at an accelerating voltage of 1−2 kV.

The surface roughness (root-mean-square (rms) roughness) was evaluated using a Mahr "stylus" profilometer (conic stylus dimension of 2 μm with a lateral resolution of 0.76 nm) along a 0.25 mm profile. Profilometry measurements were also used to confirm the thickness of the coatings.

The microstructure of the coatings and pore size and distribution were investigated using transmission electron microscopy (TEM) at the Laboratory of Nanoscopies and Spectroscopies (LANE-ICMSE, Sevilla, Spain) using an FEI FEGTEM Tecnai G2 F30 S-Twin operated at 300 kV. The microscope is equipped with an annular dark field (ADF) detector from Fischione Instruments, an SDD X-Max energy-dispersive X-ray (EDX) spectrometer detector from Oxford Instruments, and a Gatan GIF Quantum 963 energy filter. To determine the composition of the individual layers at the nanoscale, the scanning mode (STEM) was used with a probe size of less than 1 nm. Spatially resolved electron energy loss spectra (EELS) were recorded in the low-loss range over 2048 channels (0.05 eV/channel) with an integration time of 0.05 s.

Cross-sectional TEM specimens of the coatings deposited on the Si substrates were prepared using the conventional approach by mechanical polishing and dimple grinding followed by Ar+ ion milling until electron transparency was attained. Before the TEM experiments, the specimens were cleaned inside the TEM holder with Ar/O_2 plasma. The pore aspect ratio was evaluated from the TEM micrographs. The images were processed with image analysis software, and the pores were identified as well-defined dark contrast areas (see

DOI: 10.1021/acsami.5b02356
ACS Appl. Mater. Interfaces 2015, 7, 13889−13897

ref 13 for more details) that were then analyzed with the "analyze particle function" of the ImageJ software.[18] Approximately 200 pores per sample were considered.

The refraction index of the coatings was evaluated using ellipsometry on the samples deposited on the quartz substrates. The measurements were conducted in a UVISEL spectroscopic ellipsometer from HORIBA Jobin Yvon with an incidence angle of 70° and a wavelength range of 600−2100 nm with a precision of 0.01. The data were analyzed using the Deltapsi2 software that was developed by HORIBA Jobin Yvon.

2. Simulation, Design, and Characterization of the Photonic Structures. The photonic structures were designed using the quarter-wave configuration in which each optical layer thickness corresponds to one-quarter of the wavelength. The theoretical reflectance spectra of the designed multilayers were calculated using a code based on the transfer matrix method. For the two DRB structures presented in this work, the reflectance spectra were calculated for a Bragg peak centered at 1750 nm for $(HL)^7H$ sequence layers (H indicates high-*n* layer; L indicates low-*n* layer) using the refractive indices of the individual layers that were studied. In the case of the OMC with the resonant wavelength at 1650 nm, the layer sequence was $(HL)^4HLc(HL)^4H$ in which Lc is a low-index microcavity layer of the same type as Ln2. Table 2 presents the calculated thicknesses for the H, L, and Lc layers in our photonic structures using the refractive indexes measured for these layers.

Table 2. Constants for the Design of the Photonic Structures

structure	DBR1	DBR2	OMC
sequence of multilayer structure	$(H_nL_{n1})^7H_n$	$(H_nL_{n2})^7H_n$	$(H_nL_{n2})^4H_nLc(H_nL_{n2})^4H_n$
high refractive index (nH) ± 0.01	3.72 + i 0.01	3.72 + i 0.01	3.74 + i 0.01
low refractive index (nL) ± 0.01	2.77 + i 0.03	2.80 + i 0.02	2.81 + i 0.02
resonant wavelength (λ_0, nm)	1750	1750	1650
thickness of the high index layer (t_H, nm)	115	115	110
thickness of the low index layer (t_L, nm)	160	160	150
thickness of the microcavity layer (t_{Lc}, nm)			290
roughness (rms, nm)	3.5 ± 2.6	1.75 ± 0.5	5.5 ± 2.5

The experimental normal incidence specular reflectance spectra were acquired in the 1000−2500 nm range using a Fourier transform infrared spectrophotometer (Bruker IFS-66 FTIR) attached to a microscope, which operates in reflection mode with a 4× objective with a 0.1 numerical aperture (light cone angle ±5.7°).

The structure of the multilayer coatings was investigated using SEM and TEM cross-sectional views. The EDX and EELS line profiles were also performed across the multilayer for different electron probe positions in the STEM mode. To obtain the relative composition of Si and Ar, EDX spectra were recorded over 2000 channels (5 eV/channel) using an integration time of 2.5 s and a probe position step of 5 nm. Quantification was performed using the TIA software of the TECNAI F30 microscope. To detect the He signal (K-edge), the EELS spectra were recorded under similar conditions as for the individual layers with a probe position step of 1 nm.

RESULTS AND DISCUSSION

Characterization of the Individual Layers. Figure 2 presents TEM cross-sectional views of the individual porous (a, b) and dense (c) layers to be used in the design of the photonic structures. The influence of deposition gas, setup geometry, and substrate bias is shown. When He is used as the working gas without a substrate bias, a singular microstructure of closed pores oriented in the magnetron direction was obtained (see Figure 2a). In our previous works, we demonstrated that the pores are closed and incorporate a high amount of He (11, 20), we showed that the shadowing effects rule the growth mechanism responsible for the direction of the pores,[13] and we showed that changing the magnetron geometry was possible to orient the pores in a different direction.[12] The inset in Figure 2a shows in more detail the ellipsoidal shape and the size of the pores (lighter areas). Pores ranging from 2 to 40 nm in the major diameter of the ellipse are observed. If a substrate bias (−100 V) was applied during the film growth, the pores (with sizes ranging from 4 to 30 nm) became narrower, elongated, and were oriented perpendicularly to the substrate as shown in Figure 2b. As observed from the inset in Figure 2b, a more uniform pore size was also obtained. A detailed pore analysis was performed using imageJ[17] for both samples, major and minor diameters of the ellipsoidal-shaped pores were determined, and the pore aspect ratio (d_{minor}/d_{major}) was calculated. The results are presented in Figure 3. Sample L_{n1} presents higher aspect ratios than L_{n2}; therefore, the shape of the pores is more round (Figure 3a). When a bias was applied (sample L_{n2}), the d_{minor} diameters of the pores were much smaller than the d_{major}, and the aspect ratio decreased (Figure 3b). The use of Ar as the working gas, combined with the substrate bias, results in a very dense structure, as displayed in Figure 2c.

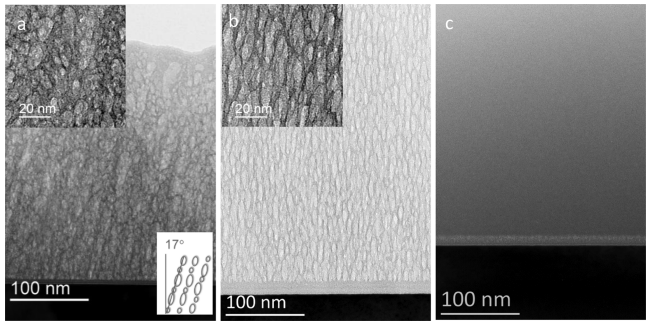

Figure 2. TEM cross-sectional views in bright field of the individual layers: (a) Sample Ln1 (without bias). (b) Sample Ln2 (with bias). (c) Sample Hn. For (a) and (b), the insets show in detail the porous structure. For (a), the additional inset shows the scheme of the pore orientation.

For the design of the single-material-photonic structures, it is essential to have high contrast in the refractive indices between the dense and porous layers while also preserving the composition. Table 1 presents the bulk composition of the coatings that was obtained by the RBS measurements. The samples were mainly composed of Si. A small amount of Ar (6 at. % Ar) was observed for the dense coating. The incorporation of Ar in the samples that were deposited via magnetron sputtering with an applied substrate bias was investigated previously by other authors;[19] nevertheless, this incorporation does not result in the introduction of porosity (more details concerning the microstructure of this dense coating are provided in reference 12).

For the porous coatings, ∼30 at. % of He was incorporated. Our previous works[12,13,20,21] prove that He is located inside the pores. Spatially resolved EELS were measured in the nanoscale regime to confirm the presence of He inside the pores (see

DOI: 10.1021/acsami.5b02356
ACS Appl. Mater. Interfaces 2015, 7, 13889−13897

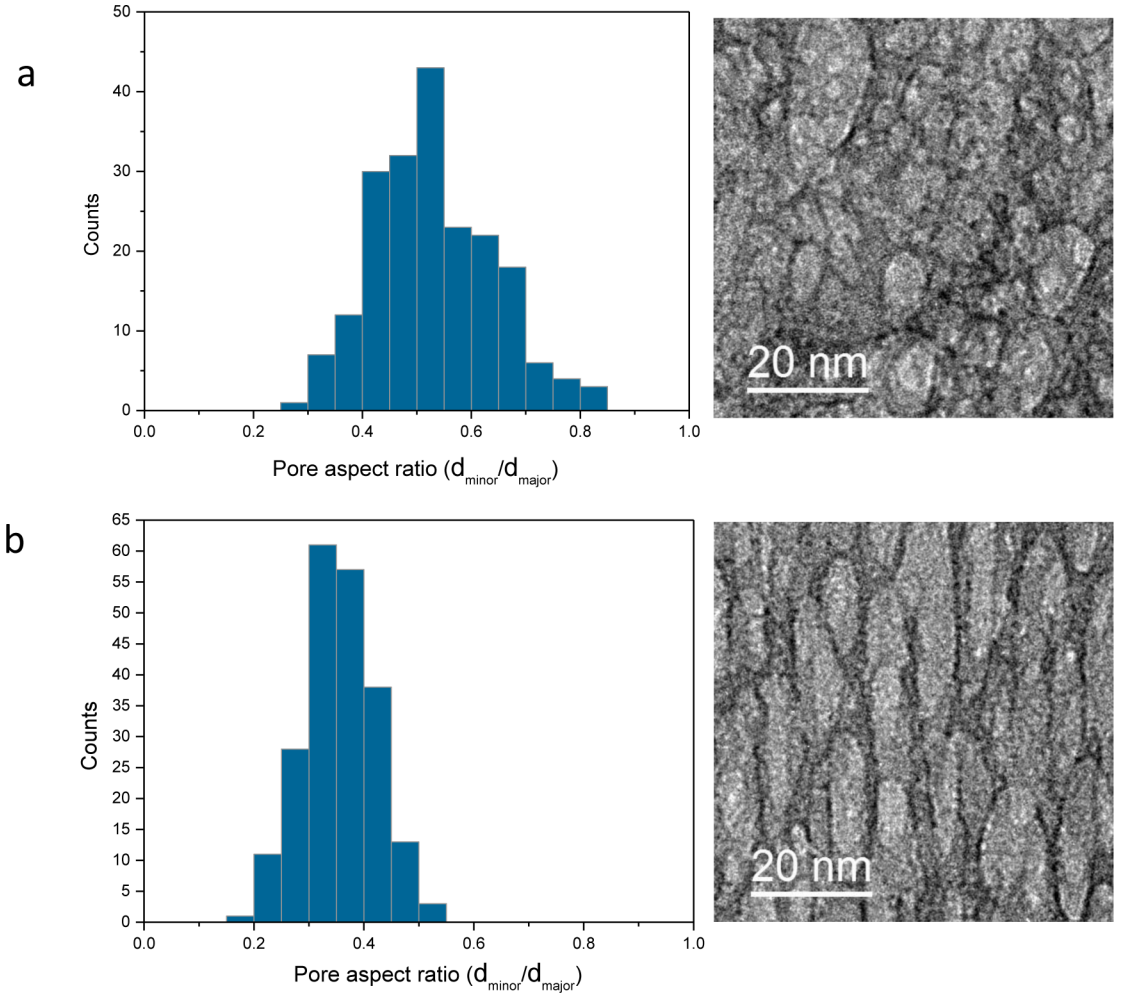

Figure 3. Pore aspect ratio (d_{minor}/d_{major}) as obtained from the TEM analysis: (a) Sample L_{n1} and (b) Sample L_{n2}.

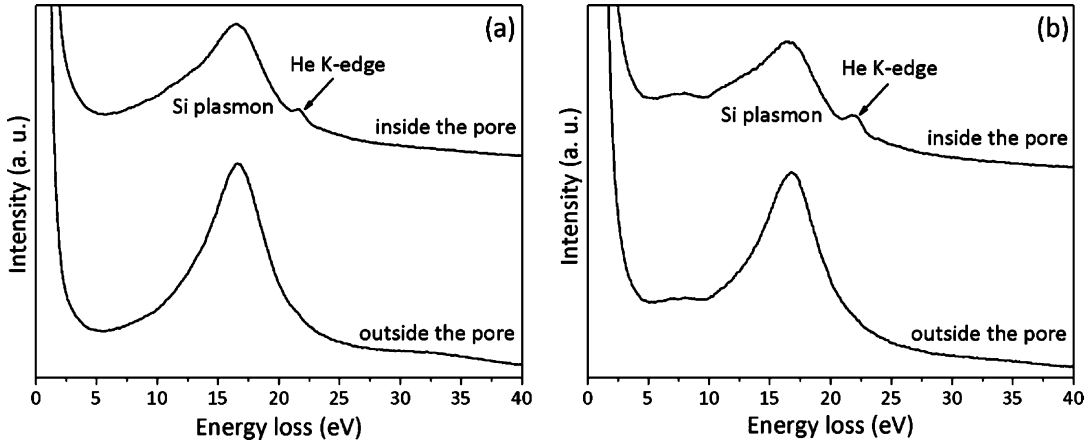

Figure 4. EELS spectra of the porous coatings corresponding to the selected areas inside and outside of the pores for (a) L_{n1} and (b) L_{n2} coatings. These spectra were obtained by aligning and summing five spectra together. The data are presented with a vertical shift for comparison purposes.

more details in ref 21). Figure 4 shows the EELS spectra of the porous coatings that correspond to a selected area at the center and outside of the pores. Except for a very small peak at ~7 eV in the L_{n2} spectra, both samples present very similar spectra. This small peak has been reported to correspond to the SiO_2/Si interface plasmon[22] that is most likely due to surface oxidation during TEM sample preparation because no oxygen signal was found in the RBS results of both samples, as displayed in Table 1.

Outside the pores, the low loss spectra for both samples contains a strong peak corresponding to the Si plasmon at 17 eV;[23] however, inside the pores a small peak appears at ~22 eV that corresponds to the He K-edge,[23] confirming the presence of He inside the pores. As previously reported, the low solubility of He causes the formation of bubbles in ion

DOI: 10.1021/acsami.5b02356
ACS Appl. Mater. Interfaces 2015, 7, 13889−13897

implanted[24−26] or sputtered metals.[27,28] More recently, plasma treatments with He incorporation via magnetron sputtering have also been suggested as a route for nanostructuring metals.[29,30]

The optical properties of these coatings were investigated by ellipsometry. Figure 5 shows the results of the refractive index

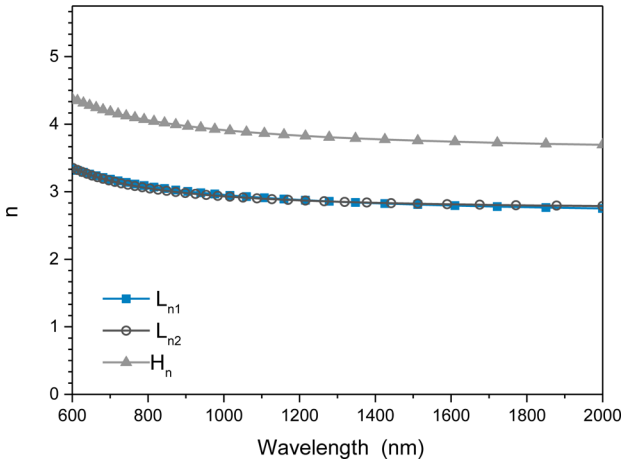

Figure 5. Refractive index (n) as a function of the wavelength of the porous (L_{n1}, L_{n2}) and dense (H_n) silicon coatings.

measurements as a function of the wavelength. As expected from the microstructure and composition results, a high contrast of the refractive index between the dense and porous layers was observed. Both porous coatings present similar n values in the measured range. In the case of the dense coating, the refractive index is high, typical of amorphous silicon.[31,32] The refractive indices for these coatings at the selected wavelength for the different photonic structures are directly compared in Table 2.

By using the refractive index of the porous coatings at the wavelength of interest and the effective medium approximations and expressing the relative electrical permittivity of a heterogeneous media ($\varepsilon_{(r,\,eff)}$) according to Maxwell−Garnett theory as a function of the dielectric constants of the continuous ($\varepsilon_{(r,\,c)}$) and the dispersed ($\varepsilon_{(r,\,d)}$) phases, we can calculate the volume fraction (ϕ) occupied by the dispersed phase and the pores, according to eq 1:[33]

$$\varepsilon_{(r,eff)} = \varepsilon_{(r,c)}\left[1 - \frac{3\phi(\varepsilon_{(r,c)} - \varepsilon_{(r,d)})}{2\varepsilon_{(r,c)} + \varepsilon_{(r,d)} + f(\varepsilon_{(r,c)} - \varepsilon_{(r,d)})}\right] \quad \text{(eq 1)}$$

Considering that the dense matrix in which the pores are embedded has the same refractive index as the dense coating ($\varepsilon_{(r,\,c)}$) and considering that the dielectric constant of the pores ($\varepsilon_{(r,\,d)}$) is 1, the porosity fraction ϕ can be estimated for these coatings (see Table 1). The values (38.9 and 41.5%) found are consistent with the published refractive index for porous silicon with a different porosity that is produced by chemical etching. When comparing our values with the ones presented by G. Korotcenkov and B. K. Cho,[2] the porous coatings have porosities between 20 and 40%, which are in good agreement with the values found by the Maxwell−Garnet equation in our coatings.

Single Material Photonic Structures by Magnetron Sputtering. Figure 6a presents the calculated and measured optical response of the two Bragg reflectors at 1750 nm that were developed in this work. Using the measured refractive index values of the coatings presented in Table 2, for an $(HL)^7H$ sequence, the calculated thicknesses for the dense and porous layers were obtained and are presented in Table 2. According to the simulations, a seven-period structure is enough to ensure a very high reflectivity (~95%). By knowing the deposition rate of the individual layers presented in Table 1 and controlling the deposition time of each layer, it is possible to grow these optical multilayers via magnetron sputtering in a single batch by changing the deposition gas. The comparison between the measurements (straight lines) and the simulation results (dashed lines) indicates not only an adequate control of the refractive index and the thickness of the layers but also that optically smooth surfaces can be obtained via this method, which was confirmed by the low roughness values, as shown in Table 2. Nevertheless, the experimental curves present slightly wider stop bands compared to the simulations that could be related to the slightly higher n contrast between the two layers that compose the DBR than was measured for the individual layers. The adjustment of the theoretical curves to the experimental values indicates that there is a slightly higher n

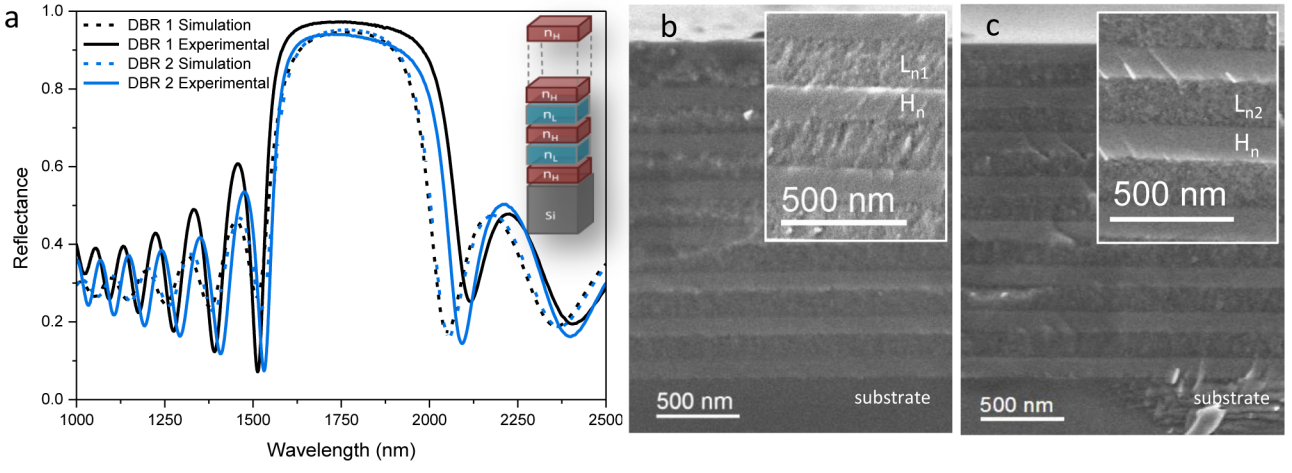

Figure 6. (a) Calculated and measured reflectance spectra for DBR1 and DBR2; SEM cross-sectional views of the (b) DBR1 and (c) DBR2 structures. (insets) Magnified micrographs of the layers.

DOI: 10.1021/acsami.5b02356
ACS Appl. Mater. Interfaces 2015, 7, 13889−13897

value for the dense layers in both Bragg reflectors: 3.93 for DBR1 and 3.8 for DBR2.

Figure 6b,c displays the SEM-FEG cross sections of the designed structures. As shown in Figure 6b, DBR1 is formed with stacks of H_n and L_{n1} (no substrate-biased porous coating) layers, and Figure 6c shows the DBR2 formed by H_n and L_{n2} (biased porous coating) layers; see design conditions in Table 2. The different contrast in the images corresponds to the dense and porous layers; the insets show in detail the morphology of these structures. In both cases, the layers in the Bragg stacks present a similar morphology to the corresponding individual layers studied before with clearly defined interfaces that are continuously repeated throughout the multilayer structure.

The quality of the optical response of these multilayer systems significantly depends on the quality of the interface between the dense and porous layers. In the TEM cross sectional image (Figure 7), the sharpness of the interfaces

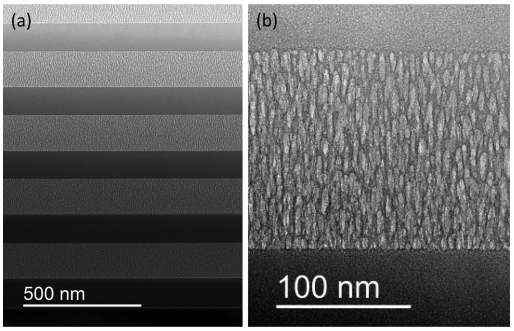

Figure 7. Bright-field TEM cross-sectional micrograph of DBR2. (a) Sharp interfaces are observed between the porous (brighter areas) and dense (darker areas) layers of the photonic structure. (b) Detail of one of the porous layers at a higher magnification.

between dense and porous silicon layers in the DBR2 is shown. Figure 7b displays a magnified image of the interface and one of the porous layers in the photonic structure. A porous structure is observed that is similar to the previously studied individual porous layer L_{n2} with vertically elongated closed pores that are perpendicular to the substrate (pore sizes from 3 to 28 nm). The chemical nature of these layers in the DBR2 was investigated in the nanoscale regime using TEM, which was also used to determine the quality of the interfaces. In Figure 8, by combining the ADF-STEM images with EDX and EELS, it is possible to attain the structural and chemical information across the different layers. In the ADF images, the intensity is proportional to the product of the square of the atomic number (Z) and the specimen thickness that is crossed by the electron beam. In Figure 8, the darker areas correspond to a lower Z, which were in this case the less dense porous layers. Additionally, the influence of the TEM specimen thickness difference was related to the sample preparation, which is observed from the substrate to the surface of the multilayer structure in Figure 8a; as the specimen becomes thinner, the image becomes darker (proportionally in dense and porous layers). The evolution of the ADF signal on the line profile across the multilayer in Figure 8a can be compared with the evolution of the Si and Ar relative composition profiles that were extracted from the EDX spectra using a standardless quantification method (He cannot be detected by EDX). The Si content is 100% for the porous layers, and it slightly decreases with the increase of Ar in the dense layer (~5 at. %),

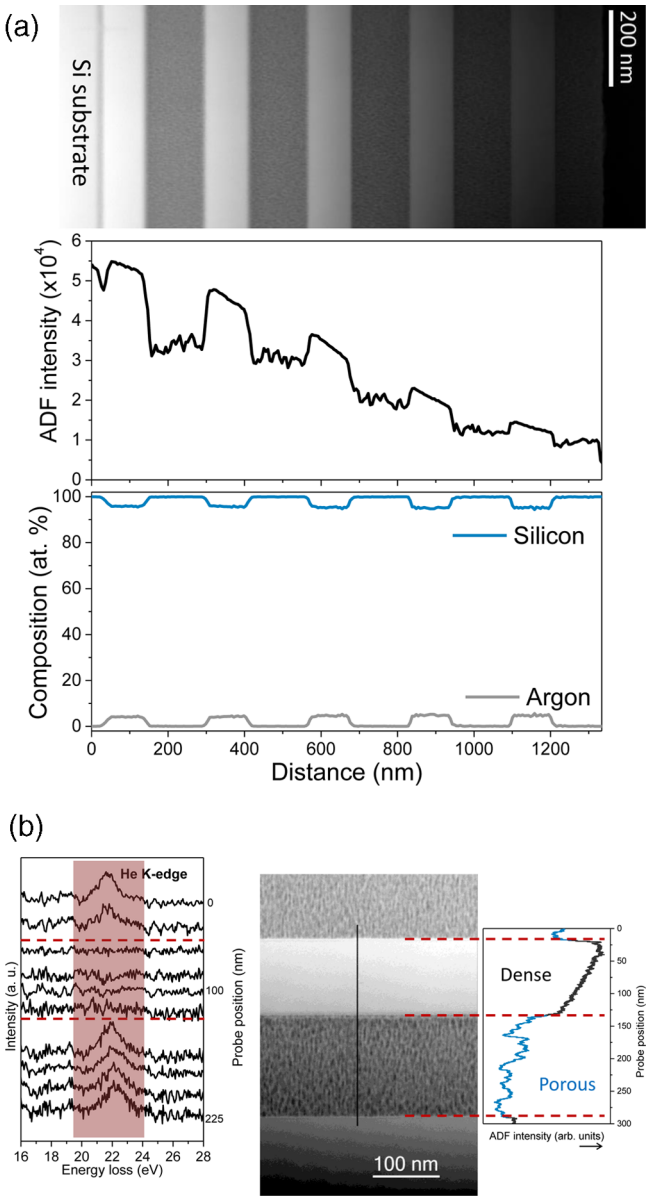

Figure 8. (a) STEM-ADF image of DBR2. The ADF signal intensity and the Si and Ar composition profiles were extracted from the STEM-EDX line profiles across the structure. (b) STEM-ADF image showing the porous and dense layers. The ADF intensity profile that was recorded across the marked line is shown on the right. The He K-edges that were extracted from the low-loss EELS spectra at a different position in the marked line are shown on the left.

similar to what measured by RBS in the individual dense layer that was characterized previously. This behavior is repeated throughout the thickness of the coating in which uniform thicknesses of dense and porous layers are pilled up with sharp interfaces.

The presence of He inside the pores of the porous layers was also investigated using the EELS profile in the nanoscale regime. Figure 8b presents the He K-edge spectra extracted from the low-loss EELS spectra at different positions in the marked line using the procedure described in Figure S1 of the Supporting Information. A detailed description of the method can be found in ref 20. An EELS spectrum along the He K-edge corresponds to each probe position across the marked line in nanometers. At positions 0 and 250 nm in the porous layers

DOI: 10.1021/acsami.5b02356
ACS Appl. Mater. Interfaces 2015, 7, 13889−13897

(lower ADF intensity), it is possible to observe the He K-edge; however, at the 100 nm position in the dense layer (higher ADF intensity), no He signal was detected.

The ADF profile is also shown on the right side of Figure 8b. We confirm that the porous layers that were integrated into the photonic structure are very similar to the individual coatings.

Because of the low deposition temperatures that are characteristic of magnetron sputtering technology, this approach could be used to produce Bragg stacks over sensible substrates, such as polymers. In Figure 9 as a proof-of-concept,

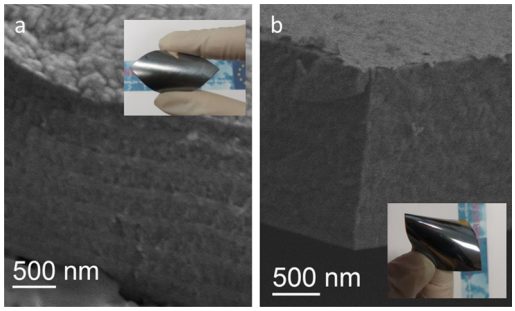

Figure 9. SEM cross-section of the DBR2 structures deposited on (a) Teflon and (b) Kapton.

we show SEM cross sections of the DBR2 deposited over Teflon (Figure 9a) and Kapton (Figure 9b). Other polymeric substrates of technological interest could be considered. The strategy presented here is proposed as an interesting straightforward method to produce single-material-multilayer structures for use in flexible silicon electronics or photonics.

By taking advantage of the oblique angle geometry and exploiting the difference in the thickness over a larger area, which is a consequence of the different distance to the magnetron, one can design graded Bragg reflectors with a controlled lateral gradient in the stop band wavelengths. Figure 10 illustrates the sample position in relation to the magnetron and the different positions measured for a large-area DBR designed using stacks of H_n and L_{n2} in a similar structure to the DBR2. Additionally, a scheme of the thickness differences obtained in the different positions from position "a" to position "d" is presented. In position "a", which is closer to the magnetron, the dense layers present a thickness of 120 nm, and the porous layer is ∼160 nm, resulting in a Bragg peak centered at 2000 nm. As one moves to position "d", the thickness of the layers decreases, and the center of the Bragg peak moves to 1468 nm with a thickness of 85 nm for the dense layer and 100 nm for the porous layer.

The methodology presented here can also be used to produce optical microcavities in which the periodicity of the Bragg stack is disrupted by the introduction of a controlled defect. In Figure 11, a porous defect layer (Lc of type L_{n2}) of ∼290 nm is introduced in the photonic structure that is designed to produce a stop band centered at 1640 nm, as predicted by the simulation. The experimentally measured reflectance spectrum reproduces the features of the calculated spectrum sufficiently. The high reflectivity band, the Bragg plateau, is ∼420 nm, and the resonance dip is very sharp with a full width at half-maximum (fwhm) of 30 nm, indicating a high *Q* factor.

CONCLUSIONS

Here, we demonstrate the fabrication of single-material optical-multilayer devices (Bragg reflectors and optical microcavities) from dense and porous (closed porosity) silicon coatings using magnetron sputtering. The influence of the substrate bias on the formation of closed porosity in the Si films that were deposited by oblique angle magnetron sputtering was investigated. The use of substrate bias results in pores aligned perpendicularly to the substrate losing the oblique angle direction. The EELS and RBS results on porous films prove the presence of He in the Si coatings located inside the closed pores. The introduction of porosity produces coatings with a reduced *n* compared to the dense coatings produced with Ar. This refractive index contrast has been used here for the production of single-material photonic multilayers via magnetron sputtering.

In this work, we have presented a simulation, a design, and the analysis of Bragg reflectors and optical microcavities. Analytical tools that are based on TEM techniques allowed a deep microstructural and chemical characterization of the layer stacks to determine the quality of the interface. Our methodology was a versatile approach, which provided adequate control over the *n* and thickness of the layer for the preparation of single-material multilayers of porous and dense Si with high-quality sharp interfaces over a wide number of layers and different types of substrates. The oblique angle geometry was explored for the production of Bragg reflectors with a controlled lateral gradient in the stop band wavelengths.

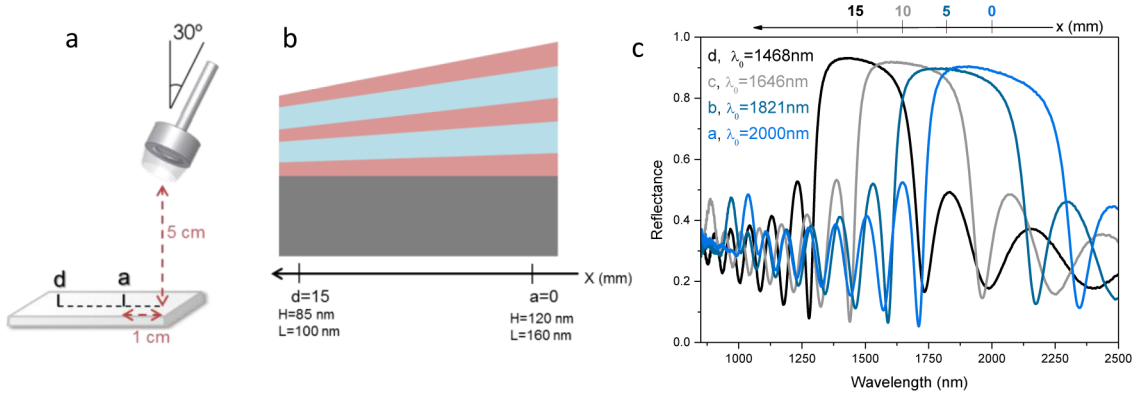

Figure 10. Gradient Bragg reflector: (a) position of the sample with respect to the magnetron, (b) sketch of the thickness difference obtained in the gradient structure, (c) reflectance spectra showing the photonic stop-band position as a function of the distance to the magnetron.

DOI: 10.1021/acsami.5b02356
ACS Appl. Mater. Interfaces 2015, 7, 13889−13897

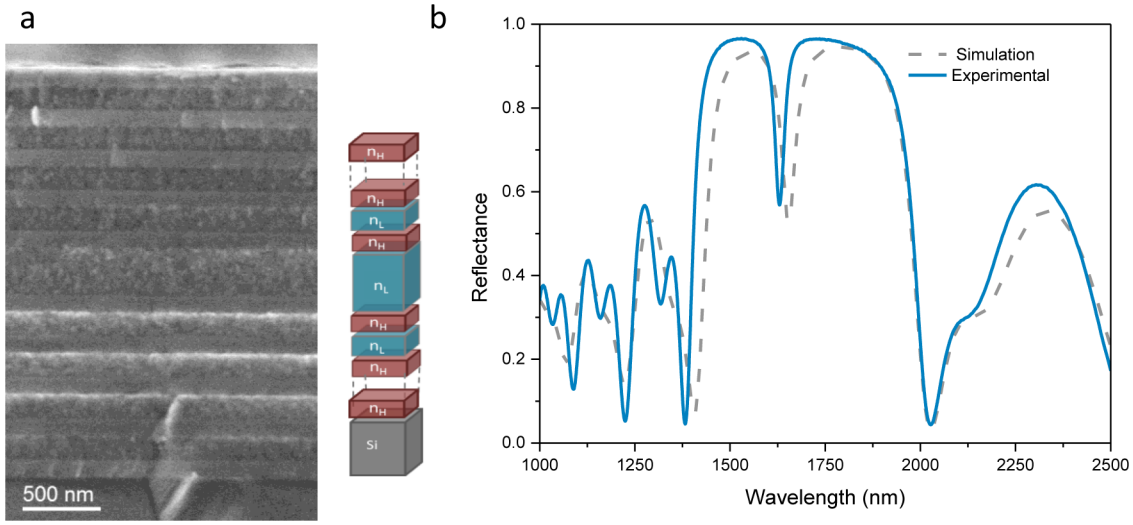

Figure 11. (a) SEM cross-sectional view of the optical microcavity and (b) the calculated and measured reflectance spectra.

■ ASSOCIATED CONTENT

Supporting Information

The extraction method of the He−K edge on the spectrum image (STEM-EELS) is described. The Supporting Information is available free of charge on the ACS Publications website at DOI: 10.1021/acsami.5b02356.

■ AUTHOR INFORMATION

Corresponding Author

*E-mail: godinho@icmse.csic.es.

Notes

The authors declare no competing financial interest.

■ ACKNOWLEDGMENTS

This work was supported by the EU 7FP (Project Al-NanoFunc CT-REGPOT-2011-1-285895, http://www.al-nanofunc.eu/), the CSIC (PIE 201060E102, PIE 201460E018), the Spanish Ministry MINECO (Project CTQ2012-32519), and Junta de Andalucía (TEP217 and PE2012-TEP862). The authors also acknowledge the Laboratory for Nanoscopies and Spectroscopies for the SEM and TEM facilities and A. Jimenez and M. Anaya for their help with the reflectivity measurements.

■ REFERENCES

(1) Yablonovitch, E. Photonic Crystals. *J. Mod. Opt.* **1994**, *41* (2), 173−194.

(2) Korotcenkov, G.; Cho, B. K. Silicon Porosification: State of the Art. *Crit. Rev. Solid State Mater. Sci.* **2010**, *35* (3), 153−260.

(3) Tokranova, N. A.; Novak, S. W.; Castracane, J.; Levitsky, I. A. Deep Infiltration of Emissive Polymers into Mesoporous Silicon Microcavities: Nanoscale Confinement and Advanced Vapor Sensing. *J. Phys. Chem. C* **2013**, *117* (44), 22667−22676.

(4) Kilian, K. A.; Böcking, T.; Gaus, K.; Gal, M.; Gooding, J. J. Peptide-Modified Optical Filters for Detecting Protease Activity. *ACS Nano* **2007**, *1* (4), 355−361.

(5) Volk, J.; Grand, T. L.; Bársony, I.; Gombkötő, J.; Ramsden, J. J. Porous Silicon Multilayer Stack for Sensitive Refractive Index Determination of Pure Solvents. *J. Phys. D: Appl. Phys.* **2005**, *38* (8), 1313.

(6) Patel, P. N.; Mishra, V. Realization of Porous Silicon Photonic Bandgap Optical Sensor Devices. *J. Optoelectron. Adv. Mater.* **2014**, *16* (3−4), 269−275.

(7) Ivanov, I. I.; Skryshevsky, V. A.; Nychyporuk, T.; Lemiti, M.; Makarov, A. V.; Klyui, N. I.; Tretyak, O. V. Porous Silicon Bragg Mirrors on Single- and Multi-Crystalline Silicon for Solar Cells. *Renewable Energy* **2013**, *55*, 79−84.

(8) Harraz, F. A.; El-Sheikh, S. M.; Sakka, T.; Ogata, Y. H. Cylindrical Pore Arrays in Silicon With Intermediate Nano-Sizes: A Template for Nanofabrication and Multilayer Applications. *Electrochim. Acta* **2008**, *53* (22), 6444−6451.

(9) Huanca, D. R.; Ramirez-Fernandez, F. J.; Salcedo, W. J. Porous Silicon Optical Cavity Structure Applied to High Sensitivity Organic Solvent Sensor. *Microelectron. J.* **2008**, *39* (3−4), 499−506.

(10) Bisi, O.; Ossicini, S.; Pavesi, L. Porous Silicon: A Quantum Sponge Structure for Silicon Based Optoelectronics. *Surf. Sci. Rep.* **2000**, *38* (1−3), 1−126.

(11) Shtenberg, G.; Massad-Ivanir, N.; Fruk, L.; Segal, E. Nanostructured Porous Si Optical Biosensors: Effect of Thermal Oxidation on Their Performance and Properties. *ACS Appl. Mater. Interfaces* **2014**, *6* (18), 16049−16055.

(12) Godinho, V.; Caballero-Hernández, J.; Jamon, D.; Rojas, T. C.; Schierholz, R.; García-López, J.; Ferrer, F. J.; Fernández, A. A New Bottom-Up Methodology to Produce Silicon Layers With a Closed Porosity Nanostructure and Reduced Refractive Index. *Nanotechnology* **2013**, *24* (27), 275604.

(13) Godinho, V.; Moskovkin, P.; Álvarez, R.; Caballero-Hernández, J.; Schierholz, R.; Bera, B.; Demarche, J.; Palmero, A.; Fernández, A.; Lucas, S. On The Formation of the Porous Structure in Nanostructured a-Si Coatings Deposited by Dc Magnetron Sputtering at Oblique Angles. *Nanotechnology* **2014**, *25* (35), 355705.

(14) Iyyakkunnel, S.; Marot, L.; Eren, B.; Steiner, R.; Moser, L.; Mathys, D.; Dueggelin, M.; Chapon, P.; Meyer, E. Morphological Changes of Tungsten Surfaces by Low-Flux Helium Plasma Treatment and Helium Incorporation via Magnetron Sputtering. *ACS Appl. Mater. Interfaces* **2014**, *6* (14), 11609−11616.

(15) Zhang, X.; Lan, P.; Lu, Y.; Li, J.; Xu, H.; Zhang, J.; Lee, Y.; Rhee, J. Y.; Choy, K.-L.; Song, W. Multifunctional Antireflection Coatings Based on Novel Hollow Silica-Silica Nanocomposites. *ACS Appl. Mater. Interfaces* **2014**, *6* (3), 1415−1423.

(16) Xu, X.; Subbaraman, H.; Chakravarty, S.; Hosseini, A.; Covey, J.; Yu, Y.; Kwong, D.; Zhang, Y.; Lai, W.-C.; Zou, Y.; Lu, N.; Chen, R. T. Flexible Single-Crystal Silicon Nanomembrane Photonic Crystal Cavity. *ACS Nano* **2014**, *8* (12), 12265−12271.

(17) Calvo, M. E.; Miguez, H. Flexible, Adhesive, and Biocompatible Bragg Mirrors Based on Polydimethylsiloxane Infiltrated Nanoparticle Multilayers. *Chem. Mater.* **2010**, *22* (13), 3909−3915.

(18) Rasband W. S. *ImageJ*; U.S. National Institutes of Health: Bethesda, MD, 2012. Online: imagej.nih.gov/ij/.

DOI: 10.1021/acsami.5b02356
ACS Appl. Mater. Interfaces 2015, 7, 13889−13897

(19) Williams, D. S.; Baiocchi, F. A.; Beairsto, R. C.; Brown, J. M.; Knoell, R. V.; Murarka, S. P. Nitrogen, Oxygen, and Argon Incorporation During Reactive Sputter Deposition of Titanium Nitride. *J. Vac. Sci. Technol., B* **1987**, *5* (6), 1723−1729.
(20) Godinho, V.; Rojas, T. C.; Fernandez, A. Magnetron Sputtered aSioxny Thin Films: A Closed Porous Nanostructure With Controlled Optical and Mechanical Properties. *Microporous Mesoporous Mater.* **2012**, *149* (1), 142−146.
(21) Schierholz, R.; Lacroix, B.; Godinho, V.; Caballero-Hernández, J.; Duchamp, M.; Fernández, A. STEM−EELS Analysis Reveals Stable High-Density He in Nanopores of Amorphous Silicon Coatings Deposited by Magnetron Sputtering. *Nanotechnology* **2015**, *26* (7), 075703.
(22) David, M. L.; Pailloux, F.; Mauchamp, V.; Pizzagalli, L. In Situ Probing of Helium Desorption from Individual Nanobubbles Under Electron Irradiation. *Appl. Phys. Lett.* **2011**, *98* (17), 171903−171903−3.
(23) Moreau, P.; Brun, N.; Walsh, C. A.; Colliex, C.; Howie, A. Relativistic Effects in Electron-Energy-Loss-Spectroscopy Observations of The Si/SiO_2 Interface Plasmon Peak. *Phys. Rev. B* **1997**, *56* (11), 6774−6781.
(24) Jäger, W.; Manzke, R.; Trinkaus, H.; Crecelius, G.; Zeller, R.; Fink, J.; Bay, H. L. Density And Pressure of Helium in Small Bubbles in Metals. *J. Nucl. Mater.* **1982**, *111−112* (0), 674−680.
(25) Walsh, C. A.; Yuan, J.; Brown, L. M. A Procedure for Measuring the Helium Density and Pressure in Nanometre-Sized Bubbles in Irradiated Materials Using Electron-Energy-Loss Spectroscopy. *Philos. Mag. A* **2000**, *80* (7), 1507−1543.
(26) Taverna, D.; Kociak, M.; Stéphan, O.; Fabre, A.; Finot, E.; Décamps, B.; Colliex, C. Probing Physical Properties of Confined Fluids within Individual Nanobubbles. *Phys. Rev. Lett.* **2008**, *100* (3), 035301.
(27) Jia, J.-p.; Shi, L.-q.; Lai, X.-c.; Wang, Q.-f. Preparation of Al Thin Films Charged With Helium by DC Magnetron Sputtering. *Nucl. Instrum. Methods Phys. Res., Sect. B* **2007**, *263* (2), 446−450.
(28) Shi, L.; Liu, C.; Xu, S.; Zhou, Z. Y. Helium-charged Titanium Films Deposited by Direct Current Magnetron Sputtering. *Thin Solid Films* **2005**, *479* (1−2), 52−58.
(29) Tanyeli, I.; Marot, L.; van de Sanden, M. C. M.; De Temmerman, G. Nanostructuring of Iron Surfaces by Low-Energy Helium Ions. *ACS Appl. Mater. Interfaces* **2014**, *6* (5), 3462−3468.
(30) Kajita, S.; Yoshida, N.; Ohno, N.; Hirahata, Y.; Yoshihara, R. Helium Plasma Irradiation on Single Crystal Tungsten and Undersized Atom Doped Tungsten Alloys. *Phys. Scr.* **2014**, *89* (2), 025602.
(31) Martin, P. J.; Netterfield, R. P.; Sainty, W. G.; McKenzie, D. R. Optical Properties of Thin Amorphous Silicon and Amorphous Hydrogenated Silicon Films Produced by Ion Beam Techniques. *Thin Solid Films* **1983**, *100* (2), 141−148.
(32) Hanyecz, I.; Budai, J.; Szilágyi, E.; Tóth, Z. Characterization of Pulsed Laser Deposited Hydrogenated Amorphous Silicon Films by Spectroscopic Ellipsometry. *Thin Solid Films* **2011**, *519* (9), 2855−2858.
(33) Hutchinson, N. J.; Coquil, T.; Richman, E. K.; Tolbert, S. H.; Pilon, L. Reflectance of Surfactant-Templated Mesoporous Silica Thin Films: Simulations Versus Experiments. *Thin Solid Films* **2010**, *518* (8), 2134−2140.

DOI: 10.1021/acsami.5b02356
ACS Appl. Mater. Interfaces 2015, 7, 13889−13897